Interface electronic engineering of molybdenum sulfide/MXene hybrids for highly efficient biomimetic sensors

Pengfei Wu[1], Tingting You[1], Qingyuan Ren[1], Hongyan Xi[1], Qingqing Liu[1], Fengjuan Qin[2], Hongfei Gu[2], Yu Wang[3], Wensheng Yan[4], Yukun Gao[1] (✉), Wenxing Chen[2] (✉), and Penggang Yin[1] (✉)

[1] *Key Laboratory of Bio-inspired Smart Interfacial Science and Technology of Ministry of Education, School of Chemistry, Beihang University, Beijing 100191, China*

[2] *Energy & Catalysis Center, School of Materials Science and Engineering, Beijing Institute of Technology, Beijing 100081, China*

[3] *Shanghai Synchrotron Radiation Facility, Zhangjiang Laboratory, Shanghai Advanced Research Institute, Chinese Academy of Sciences, Shanghai 201204, China*

[4] *National Synchrotron Radiation Laboratory, University of Science and Technology of China, Hefei 230029, China*

ABSTRACT

Interface regulation plays a key role in the electrochemical performance for biosensors. By controlling the interfacial interaction, the electronic structure of active species can be adjusted effectively at micro and nano-level, which results in the optimal reaction energy barrier. Herein, we propose an interface electronic engineering scheme to design a strongly coupled 1T phase molybdenum sulfide (1T-MoS_2)/MXene hybrids for constructing an efficient electrocatalytic biomimetic sensor. The local electronic and atomic structures of the 1T-MoS_2/$Ti_3C_2T_X$ are comprehensively studied by synchrotron radiation-based X-ray photoelectron spectroscopy (XPS), as well as X-ray absorption spectroscopy (XAS) at atomic level. Experiments and theoretical calculations show that there are interfacial stresses, atomic defects and adjustable bond-length between MoS_2/MXene nanosheets, which can significantly promote biomolecular adsorption and rapid electron transfer to achieve excellent electrochemical activity and reaction kinetics. The 1T-MoS_2/$Ti_3C_2T_X$ modified electrode shows ultra high sensitivity of 1.198 µA/µM for dopamine detection with low limit of 0.05 µM. We anticipate that the interface electronic engineering investigation could provide a basic idea for guiding the exploration of advanced biosensors with high sensitivity and low detection limit.

KEYWORDS

MXene, molybdenum sulfide, interface electronic effect, biomimetic sensor, X-ray absorption spectroscopy

1 Introduction

With the rapid development of intelligent medicine, biosensors have attracted extensive attention because they can effectively monitor the biological and medical information *in vivo* [1–6]. Dopamine (DA) is a neurotransmitter in human body, and it is considered to be an important biomarker of Parkinson's disease, schizophrenia, attention deficit hyperactivity syndrome and other diseases [7–9]. Therefore, DA detection is very important for the health diagnosis. Up to now, various methods for detecting DA have been developed, where enzyme-based biosensor through electrochemical pathway represents one of the most vital strategies because of the miniaturization, fast speed, high sensitivity and low cost [10–12]. However, the expensive price, poor stability and difficult preservation of enzymes limited the practical applications. Due to the unique physicochemical features, the functional nanomaterial-enabled signal amplification method has made some impressed breakthroughs in biosensing field [13–18]. Nevertheless, the sensitivity and selectivity still need to be further improved, which attribute to the low density of exposed active sites on electrode materials [19, 20]. Three-dimensional (3D) nanomaterial hybrids containing multiple active species

demonstrate distinctive advantages in catalytic activity and selectivity for a variety of catalytic reactions [21–24]. As a consequence, the 3D multiple nanomaterial hybrid-enabled signal amplification strategy holds great promise in DA electrochemical biosensors, which may display satisfactory sensitivity and selectivity with the assistance of tunable interface interactions, coordination environments and geometric/electronic structures of active sites.

Two-dimensional metal chalcogenides (TDMCs) have experienced major development in the pursuit of novel catalyst designs due to their controllable and rich electronic structure [25–30]. Generally, surface modification, defect engineering and heteroatom doping are common methods to design the inherent electronic structure of TDMCs [31–33]. For example, modified ions (such as F, H⁺, Cl, etc.) on the surface of TDMCs can effectively improve the carrier density, and atomic doping plays a synergistic role to achieve the enhancement of catalytic performance [34–43]. However, how to accurately manipulate their electrophilic/nucleophilic properties for bioactive catalysis is still a grand challenge. As a potential project to overcome the obstacle, the interfacial engineering modification, which is carried out through the hybrid structure formed by TDMCs, could bring

more possibilities for modifying the atomic and electronic states to improve the electrophilic/nucleophilic features of the catalysts [44–48]. The well-designed TDMC hybrid structure may lead to spontaneous electron transfer across the interface, which enhances the electron affinity of the catalytic surface and greatly improves the catalytic activity and selectivity. Especially, MXene is a graphene-like two-dimensional layered metal carbons or nitrides with rich functional groups (−F and −OH), making them perfect alternatives for coupling with TDMCs [49–51]. These unique surface structures of MXene may provide new opportunities to change the electronic structure of two-dimensional (2D) nano materials and maintain the integrity of their matrix.

In this work, we establish a providential MoS_2/MXene hybrid structure through interface electronic engineering for efficient electrocatalytic biomimetic sensors. The atomic interface effects are demonstrated by systemative X-ray spectroscopies through synchrotron radiation facility at Mo K-edge, Mo L-edge, S L-edge, Ti L-edge, etc. The strong electronic coupling and interfacial stress between $1T-MoS_2$ and $Ti_3C_2T_X$, cause the shortening of the Mo-S bond-length and accordingly accelerates the reaction kinetics as an electron transfer channel. In addition, the 3D structures provide more active sites for biomolecular adsorption. As results, the MoS_2/MXene hybrid exhibits a high detection limit for DA (1.198 μA/μM in the range of 0.1 to 40 μM) and a low limit of detection (0.05 μM). This work provides practical pathway for the rational design of efficient biomimetic sensors by applying two-dimensional hybrid materials.

2   Result and discussion

2.1   Preparation and characterization

The preparation process of $1T-MoS_2$/$Ti_3C_2T_X$ hybrid was schemed in Fig. 1. Firstly, the aluminium layer in Ti_3AlC_2 MAX phase was etched with LiF and HCl (Fig. S1 in the Electronic Supplementary Material (ESM)). Then, the few-layer $Ti_3C_2T_X$ was obtained by ultrasonic centrifugal peeling. The Tyndall scattering effect of few-layer $Ti_3C_2T_X$ nanosheets was also observed (Fig. S2(a) in the ESM). Finally, $1T-MoS_2$/$Ti_3C_2T_X$ was obtained by a hydrothermal process where $1T-MoS_2$ was grown *in-situ* on the surface of $Ti_3C_2T_X$. The abundant functional groups in $Ti_3C_2T_X$ provided a lot of anchor sites for the uniform growth of $1T-MoS_2$ [52–54]. In addition, the −OH group on the surface of $Ti_3C_2T_X$ had good hydrophilicity, which made Mo^{6+} first adsorb on the surface for nucleation and growth, and prevented the re accumulation of MoS_2 sheets [55–58]. The MoS_2/$Ti_3C_2T_X$ composite was generated and settled to the bottom (Fig. S2(b) in the ESM), which acted as the working electrode of the bionic sensor (Figs. S2(c) and S2(d) in the ESM). Figure 2(a) and Fig. S3 showed the scanning electron microscopy (SEM) image of the prepared $1T-MoS_2$/$Ti_3C_2T_X$. It was found that $1T-MoS_2$ nanosheets stood closely on $Ti_3C_2T_X$ with random orientation and bending features. The $1T-MoS_2$ and $Ti_3C_2T_X$ nanosheets were also prepared and characterized in Figs. S4–S7 in the ESM as contrast samples [55]. According to high-resolution TEM (HRTEM) image in Fig. 2(b), the interlayer spacing of $Ti_3C_2T_X$ and $1T-MoS_2$ is 0.24 and 0.62 nm, respectively. Interestingly, the lattice at the interface become larger, resulting from the atomic coupling between $Ti_3C_2T_X$ and $1T-MoS_2$. Remarkably, there are hexagonal lattice and triangular lattice in the same plane, suggesting $1T-MoS_2$ is successfully obtained by *in-situ* growth process (Figs. S8–S10 in the ESM). In addition, the element mapping of the electrode material (Fig. 2(c)) showed that $1T-MoS_2$ nanosheets grow uniformly on the surface of $Ti_3C_2T_X$. The SEM and TEM results suggested the tight binding between $Ti_3C_2T_X$ and $1T-MoS_2$ nanosheets bending regions. X-ray diffraction (XRD) and Raman characterizations further proved that the synthesized sample was a complex of $1T-MoS_2$ and $Ti_3C_2T_X$ (Fig. S11 in the ESM). Interestingly, in the Raman spectroscopy, the A_{1g} peak of $1T-MoS_2$/$Ti_3C_2T_X$ obviously shifted from 405 to 399 cm^{-1}, compared with that of $1T-MoS_2$, which might be derived from the strong coupling of MoS_2 and $Ti_3C_2T_X$. In order to study the utilization efficiency of three-dimensional cross-linking of $1T-MoS_2$/$Ti_3C_2T_X$, the nitrogen isotherm and pore size distribution were obtained (Fig. S12 in the ESM), showing a higher specific surface area of 89 m²/g. compared with pure $Ti_3C_2T_X$ (5 m²/g) and $1T-MoS_2$ (38 m²/g), this good morphological feature would be conducive to the adsorption of biomolecules and provide a large number of active sites for enhanced electrochemical behavior.

For the sake of studying the chemical state of $1T-MoS_2$/$Ti_3C_2T_X$ composites, synchrotron radiation based XPS measurements were carried out. In the survey scan spectrum of $1T-MoS_2$/$Ti_3C_2T_X$ (Fig. S13 in the ESM), an obvious O signal was observed, indicating the partial oxidation of $Ti_3C_2T_X$ [56]. Before and after in-situ growth of $1T-MoS_2$, the peaks of Mo 3d, S 2p and Ti 2p all shifted to high energy, which mean that interface bonds were formed between $Ti_3C_2T_X$ and $1T-MoS_2$, in other words, a heterostructure was constructed. The XPS spectrum deconvolution of Mo 3d (Fig. 2(d) in the ESM) was three peaks. The two peaks at 232.6 and 229.5 eV of Mo 3d spectrum belong to Mo $3d_{3/2}$ and Mo $3d_{5/2}$, respectively, while those at 236.2 eV was attributed to the existence of Mo^{4+} oxidation state [57, 58]. A reasonable explanation was that unsaturated coordinated sulfur atoms was introduced into MoS_2 layer, which was also confirmed by S 2p spectrum (Fig. 2(e)). In addition to the binding energies of S $2p_{1/2}$ and S $2p_{3/2}$, there are two other peaks generated at 162.7 and 163.8 eV and assigned to the binding of apical S^{2-} or bridging disulfide S^{2-}_2 ligands [59].
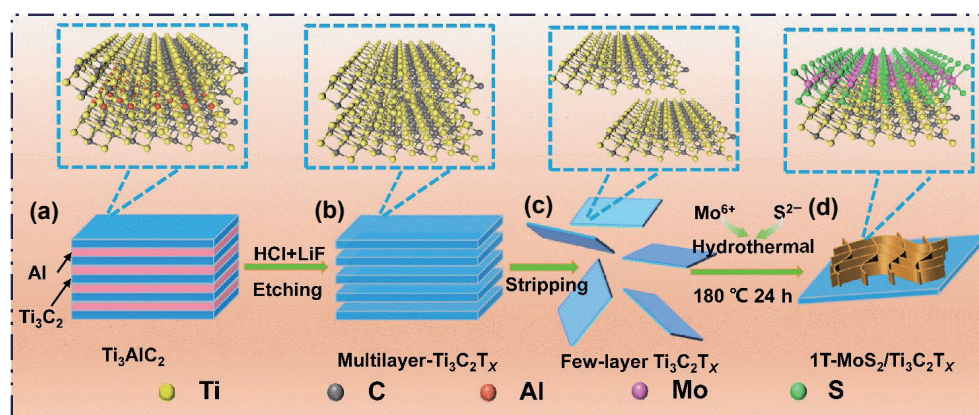

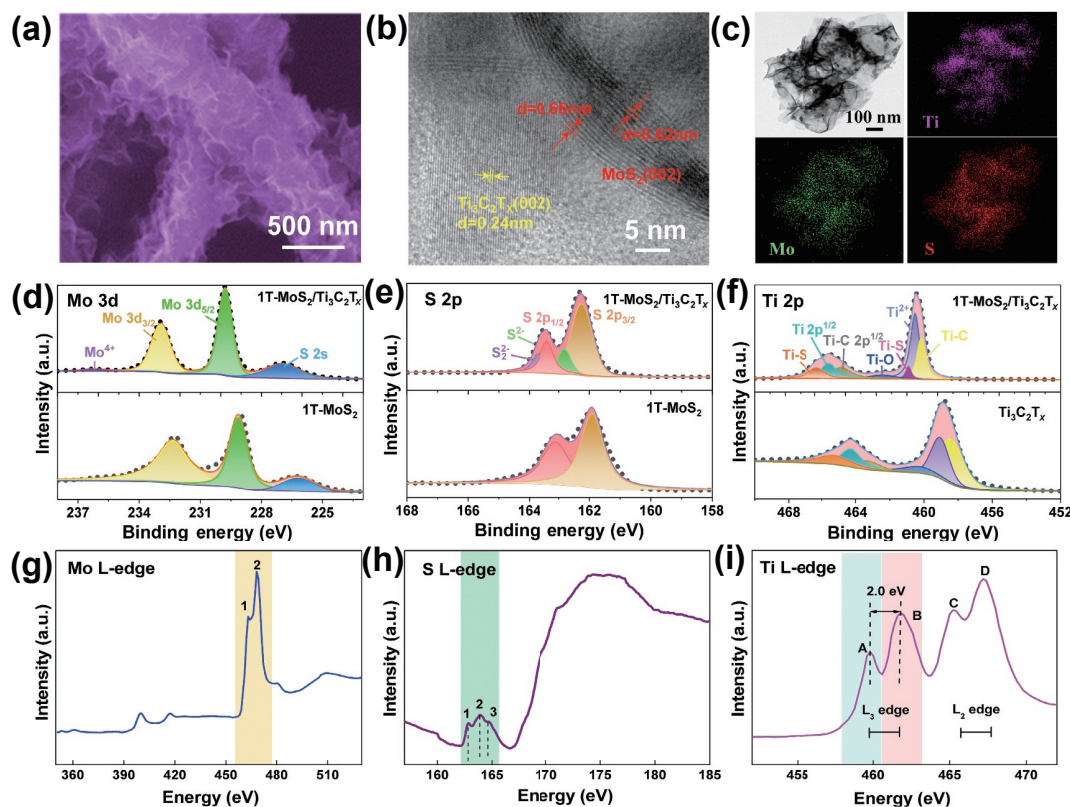**Figure 1**   Schematic of fabrication process of $1T-MoS_2$/$Ti_3C_2T_X$.

Figure 2 (a) SEM image of 1T-MoS$_2$/Ti$_3$C$_2$T$_X$. (b) HRTEM images of 1T-MoS$_2$/Ti$_3$C$_2$T$_X$. (c) EDS elemental mappings of Mo, S, and Ti. XPS spectra of the 1T-MoS$_2$/Ti$_3$C$_2$T$_X$: (d) Mo 3d, (e) S 2p, and (f) Ti 2p. (g) Mo L-edge XANES, (h) S L-edge XANES and (i) Ti L-edge XANES of 1T-MoS$_2$/Ti$_3$C$_2$T$_X$.

Figure 2(f) showed the Ti 2p spectra of 1T-MoS$_2$/Ti$_3$C$_2$T$_X$ and Ti$_3$C$_2$T$_X$. It was worth to note that there were two small peaks of 459.8 and 465.8 eV in 1T-MoS$_2$/Ti$_3$C$_2$T$_X$, belonging to Ti-S-Mo bonds [60]. The formation of these bonds also provided strong evidences for the formation of strongly connected 1T-MoS$_2$/Ti$_3$C$_2$T$_X$ interface.

In order to more deeply explore the interaction between electrons and atoms in the 1T-MoS$_2$/Ti$_3$C$_2$T$_X$ hybrids, we studied the soft XANES spectra of Mo L-edge, S L-edge and Ti L-edge of the sample, which is sensitive to the chemical elements and electronic band structure. In Fig. 2(g), the origin of the Mo L-edge XANES is mainly the electron conduction band formed by the transition of electrons from the nuclear level (3d$_{3/2}$) to the empty 4d state. In Fig. 2(h), the pre-edge of S L-edge showed three different peaks, which could be fitted with the component of spin orbit splitting, indicating that there were three dominant transitions, in which the transition energies of S 2p$_{3/2}$ component were 162.4, 163.5 and 164.35 eV, respectively. Due to the high covalence of molecular orbital, the obtained 1T-MoS$_2$/Ti$_3$C$_2$T$_X$ showed a broadened peak in this region and slightly transfered to higher energy. This indicates that sulfur existed in the unsaturated form of top S^{2-} or bridged disulfide S$_2^{2-}$ coordination, suggesting that Mo-S or Ti-S bonds might be formed, which was consistent with the results of XPS. The characteristic peaks from A to D in the Ti L-edge spectrum (Fig. 2(i)) indicated the transition of Ti 2p electrons to unoccupied three-dimensional electronic states. Peak A and peak B were located at 458.2 and 460.2 eV respectively, reflecting the L$_3$ edge transition from 2p$_{3/2}$ to 3d$_{5/2}$, in which the energy gap of 2.0 eV showed the characteristics of anatase structure. Features C and D at 463.6 and 465.7 eV belonged to L$_2$ edge transition from 2p$_{1/2}$ to 3d$_{3/2}$ state [61]. The above analysis revealed that the sulfur rich unsaturated site in MoS$_2$ and the strong electronic coupling between Ti$_3$C$_2$T$_X$ and sulfur provided a large number of catalytically active sites. This strong conjugate bond could not only effectively alleviate the self agglomeration of nanosheets, but also act as an electron bridge at the 1T-MoS$_2$/Ti$_3$C$_2$T$_X$ heterogeneous interface.

The structure of 1T-MoS$_2$ was further studied at the atomic level by synchrotron radiation hard X-ray absorption fine structure (XAFS) measurement. In general, the average oxidation state of Mo element can be described by the absorption threshold position of Mo K-edge [62]. In the XANES curve (Fig. 3(a)), the position of the sample was between Mo$_2$C and bluk MoS$_2$, indicating that the oxidation state of Mo is between the two references. As we all know, Fourier transform (FT) is a basic step of EXAFS spectral data extraction and interpretation. The FT-EXAFS of the samples were shown in Fig. 3(b) and Fig. S14 in the ESM. We found that the 1T-MoS$_2$/Ti$_3$C$_2$T$_X$ had two FT peaks at 1.9 and 2.5 Å, which was mainly due to the scattering of the first shell Mo-S and the second shell Mo-Mo coordination [63]. Compared with bulk MoS$_2$, the peak strengths of Mo-S bond and Mo-Mo bond decreased significantly. This reduced Mo-S bond length and Mo-Mo bond coordination number were typical characteristics of 1T phase [64]. Moreover, the ultra-small size of 1T-MoS$_2$ further reduced the coordination number. The nearest Mo-S bond length was slightly shorter, which might be due to the defects caused by solvothermal treatment or interface effect in the heterojunction structure. Wavelet transform (WT) is considered as a good supplement to FT because of its strong resolution in *k* and *R* space. The Mo K-edge WT-EXAFS of the sample was shown in Fig. 3(c) and Fig. S15 in the ESM. The WT contour map of the sample had only one strength maximum at 4.2 Å, corresponding to the Mo-S bond [65]. The structural parameters were quantitatively fitted by EXAFS. The fitting results were shown in Figs. 3(d) and 3(e), Fig. S16 and Table S1 in the ESM. Based on EXAFS fitting, it was considered that Mo-S bond shrinks and shortens the electron transmission distance.

2.2 Electrochemical properties

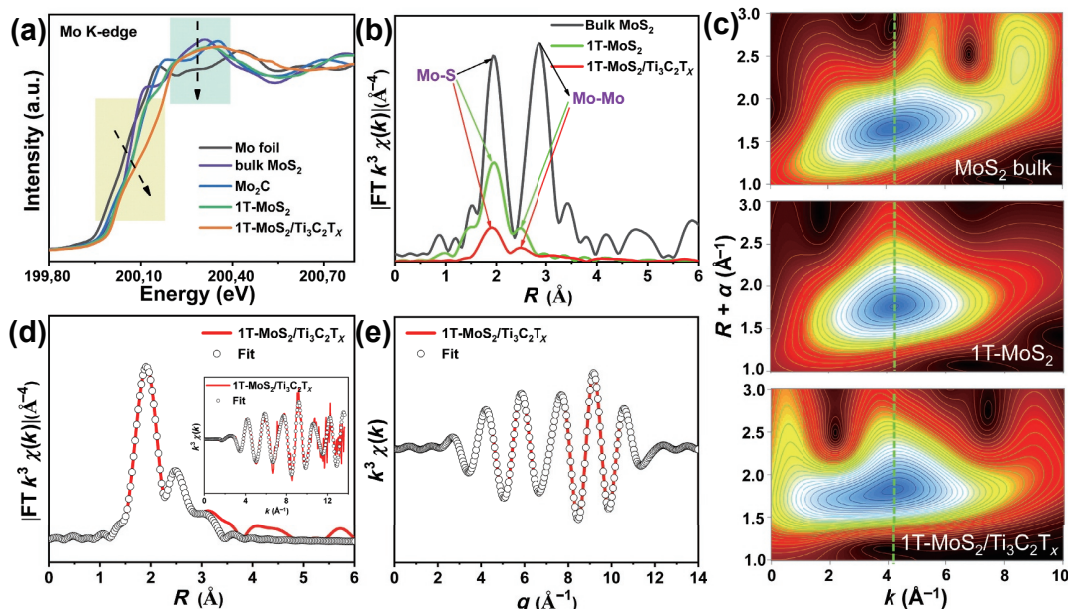Cyclic voltammetry (CV) method was used to detect DA on indium tin oxide (ITO) bare electrode, Ti$_3$C$_2$T$_X$, 1T-MoS$_2$ and 1T-

Figure 3 (a) The experimental Mo K-edge XANES spectra of 1T-MoS$_2$/Ti$_3$C$_2$T$_X$ and the references (Mo foil, bulk MoS$_2$, Mo$_2$C and 1T-MoS$_2$). (b) Fourier transfers of the k^3-weighted EXAFS oscillations of the as-prepared samples. (c) Wavelet transforms for the k^2-weighted Mo K-edge EXAFS signals of bulk MoS$_2$, 1T-MoS$_2$ and 1T-MoS$_2$/Ti$_3$C$_2$T$_X$, respectively. (d) FT-EXAFS fitting curves of 1T-MoS$_2$/Ti$_3$C$_2$T$_X$ and the Corresponding Mo K-edge EXAFS fitting curves. (e) q space fitting curve at Mo K-edge.

MoS$_2$/Ti$_3$C$_2$T$_X$ electrode, as shown in Fig. S17 in the ESM. The oxidation peak potential of DA was about 0.2 V. Compared with the bare electrode, the oxidation peak current of 1T-MoS$_2$/Ti$_3$C$_2$T$_X$ electrode was obviously increased. The possible reasons were as follows: (1) 1T-MoS$_2$ nanosheets uniformly grown on the Ti$_3$C$_2$T$_X$ MXene framework had high conductivity (Fig. S18 in the ESM) and electrocatalytic properties. (2) The 1T-MoS$_2$/Ti$_3$C$_2$T$_X$ electrode had a large electrochemically active area of 2.19 cm^2 (Fig. S19 in the ESM). (3) The 1T-MoS$_2$/Ti$_3$C$_2$T$_X$ electrode had improved wettability (Fig. S20 in the ESM), which was conducive to increasing the contact between active sites and biomolecules. (4) The synergistic effect of Ti$_3$C$_2$T$_X$ MXene and 1T-MoS$_2$ further improved the electrochemical performance of the electrode.

The effect of scanning rate on the CV reaction of DA was studied under 1T-MoS$_2$/Ti$_3$C$_2$T$_X$ condition. As shown in Fig. 4(a), with the increase of scanning rate (40–500 mV/s), the redox current density intensity of DA increased, and the peak potential gradually shifted to a positive value. Obvious oxidation and reduction peaks were observed, indicating that the electrode reaction of DA was quasi reversible. The linear relationship between the peak current density and the square root of scanning rate indicated that the oxidation of DA on 1T-MoS$_2$/Ti$_3$C$_2$T$_X$ was a diffusion controlled process (Fig. 4(b)) [66]. Compared with CV, the charging current of DPV had less influence on the background current, so DPV was selected to accurately obtain the electrode sensitivity. Figure 4(c) showed the DPV curve of 1T-MoS$_2$/Ti$_3$C$_2$T$_X$ electrode in DA at different concentrations. With the increase of DA concentration, the oxidation peak current of DA increased. The linear equation was (R^2 = 0.999) (Fig. 4(d)). The sensitivity of 1T-MoS$_2$/Ti$_3$C$_2$T$_X$ electrode was 1.198 µA/µM. The LOD was 0.05 µM (S/N = 3) (Fig. S21 in the ESM). As shown in Table S2 in the ESM, the performance of 1T-MoS$_2$/Ti$_3$C$_2$T$_X$ electrode was better than that reported previously. Other potential interference sources were also used as interference items. Through the interference test, as shown in Fig. S22(a) in the ESM, it can be seen that there is no response current change with the addition of the interference source, but a large current change is detected when DA is added. In addition, we also conducted the DPV test of interference source, and its peak current at the same potential is shown in Figs. S22(b) and
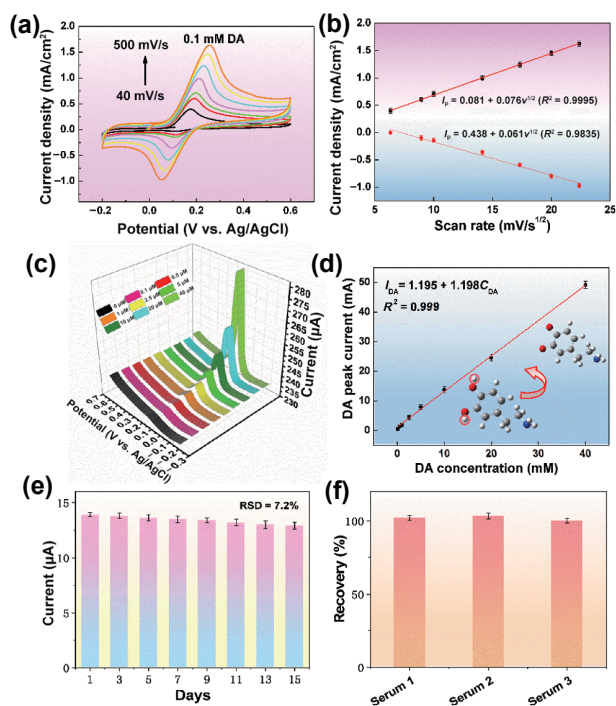

Figure 4 (a) CV curves of 1T-MoS$_2$/Ti$_3$C$_2$T$_X$ electrode in 0.1 mM DA with different sacnning rates of 40, 80, 100, 200, 300, 400 and 500 mV/s. (b) Relationship of the DA oxidation peak current density vs. the square-root of the scan rate in the range of 40–500 mV/s. (c) DPV curves of the 1T-MoS$_2$/Ti$_3$C$_2$T$_X$ electrode in DA with different concentrations. (d) Relationship of the DA oxidation peak current *vs.* its concentration. (e) Stability of 1T-MoS$_2$/Ti$_3$C$_2$T$_X$ for DA detection with a long lifetime. (f) Recovery investigation of 1T-MoS$_2$/Ti$_3$C$_2$T$_X$ performed by adding standard DA in human serum samples.

S22(c) in the ESM. It can be seen that the sensitivity of materials to DA is the best under the same conditions, indicating that 1T-MoS$_2$/Ti$_3$C$_2$T$_X$ electrode has a high selection for DA molecules. More importantly, repeatability and stability are important indicators of sensing materials, so we repeated DPV test on 1T-MoS$_2$/Ti$_3$C$_2$T$_X$ nanosheets electrode for 6 times in 10 µM DA andfour different 1T-MoS$_2$/Ti$_3$C$_2$T$_X$ electrodes (Fig. S23 in the

ESM). It was found that the oxidation peak of DA had no significant change, indicating that it had good inter-assay and intra-assay repeatabilities. In addition, DPV test was carried out every two days to test its long-term stability (Fig. 4(e)). The results showed that the peak current decreased less than 7.2% after two weeks, indicating that 1T-MoS_2/$Ti_3C_2T_X$ electrode had good stability. The 1T-MoS_2/$Ti_3C_2T_X$ was characterized after the catalytic reaction (Fig. S24 in the ESM). TEM and HRTEM can see obvious lattice stripes of MoS_2 and $Ti_3C_2T_X$. XRD shows that no new phase appears. EDS map shows the uniform distribution of Mo, S, Ti and C, indicating that the 1T-MoS_2/$Ti_3C_2T_X$ has good structural stability.

In order to test the feasibility of the electrode in the actual sample, we selected the urine of healthy human as the sample and diluted the urine 500 times with 0.01 M PBS. As shown in Fig. 4(f), the recoveries of DA at different concentrations ranged from 100.2% to 103.4%. The RSD of five parallel tests was less than 2.0% (Table S3 in the ESM). The results show that 1T-MoS_2/$Ti_3C_2T_X$ electrode can be used for the detection of DA in urine, which has a great clinical application prospect.

3 Theoretical calculations

To demonstrate the sensing behavior of 1T-MoS_2/$Ti_3C_2T_X$ heterogeneous interface, density functional theory (DFT) was used for calculation. As can be seen from Fig. 5(a), the adsorption energy (E_{ads}) value of DA adsorbed on 1T-MoS_2/$Ti_3C_2T_X$ is lower than that of MoS_2 and $Ti_3C_2T_X$, indicating that DA has good adsorption and stronger interaction with 1T-MoS_2/$Ti_3C_2T_X$. Therefore, we also studied the surface electronic structure of hybrid heterostructures. The calculation results show that MoS_2 has typical semiconductor properties (Fig. 5(b)). It is worth noting that the Density of states (DOS) intensity of 1T-MoS_2/$Ti_3C_2T_X$ is higher than that of 1T-MoS_2 at the Fermi level. Therefore, 1T-MoS_2/$Ti_3C_2T_X$ is more conducive to charge transfer, which is

consistent with the results of electrochemical properties. From the DOS of the active group (OH) of DA (Fig. 5(c)), 1T-MoS_2/$Ti_3C_2T_X$ makes DA move closer to the Fermi level, indicating that there is a strong hybridization between DA and the substrate [67]. From the charge density of DA on different substrates, there is a small amount of charge transfer in MoS_2 and $Ti_3C_2T_X$, while there is more charge transfer on the surface of 1T-MoS_2/$Ti_3C_2T_X$ (Fig. 5(d)), indicating that the electron interaction is stronger in 1T-MoS_2/$Ti_3C_2T_X$ system. In conclusion, the DA detection performance of 1T-MoS_2/$Ti_3C_2T_X$ heterogeneous interface is mainly due to its large electroactive specific surface area and high electron transfer ability.

4 Conclusion

In conclusion, we rationally designed a molybdenum sulfide/MXene hybrids with strong electronic coupling through practical hydrothermal strategy, in which 1T-MoS_2 was grown *in-situ* on the surface of $Ti_3C_2T_X$. The interface effects were appropriately monitored by comprehensively synchrotron radiation-based X-ray spectroscopy, as well as transmission electron microscopy. The highly correlated 3D heterogenous structures established effective charge transfer channels and active sites on 1T-MoS_2 nanosheets. The novel 1T-MoS_2/$Ti_3C_2T_X$ electrode exhibited remarkable performance in the ultra sensitive detection of dopamine. We expect that the interface electronic strategy could provide a basic idea for guiding the investigations of advanced biosensors with high sensitivity and low detection limit.

Electronic Supplementary Material: Supplementary materials (materials and characterization, XAFS measurements and XAFS data analysis, additional SEM images, XRD patterns, TEM images, EDX spectrum, robustness results, kinetic analysis, dosage-response curve) is available in the online version of this article at https:// doi.org/10.1007/s12274-022-5038-3.

Figure 5 Theoretical simulation for DA at MoS_2/$Ti_3C_2T_X$ MXene heterointerface. (a) DA adsorption and the corresponding adsorption energy at MoS_2, $Ti_3C_2T_X$ and MoS_2/$Ti_3C_2T_X$ MXene heterointerface (Inset: computational models). (b) DOS plots (fermi levels are set as zero and indicated with dashed lines) of MoS_2, $Ti_3C_2T_X$ and MoS_2/$Ti_3C_2T_X$ (c) The DOS of the isolated DA molecule and adsorption on MoS_2, $Ti_3C_2T_X$ and MoS_2/$Ti_3C_2T_X$. The dotted line represents the Fermi energy, which is assigned a value of zero. (d) Electron density differences for DA absorbed on the (1) MoS_2, (2) $Ti_3C_2T_X$ and (3) MoS_2/$Ti_3C_2T_X$. in which the red and green areas represent the charge accumulation and charge depletion, respectively.

References

[1] Herud-Sikimić, O.; Stiel, A. C.; Kolb. M.; Shanmugaratnam, S.; Berendzen, K. W.; Feldhaus, C.; Höcker, B.; Jürgens, G. A biosensor for the direct visualization of auxin. *Nature* 2021, *592*, 768–772.

[2] Inda, M. E.; Lu, T. K. Microbes as biosensors. *Annu. Rev. Microbiol.* 2020, *74*, 337–359.

[3] Kim, J.; Campbell, A. S.; de Ávila, B. E. F.; Wang, J. Wearable biosensors for healthcare monitoring. *Nat. Biotechnol.* 2019, *37*, 389–406.

[4] Xiong, C.; Tian, L.; Xiao, C. C.; Xue, Z. G.; Zhou, F. Y.; Zhou, H.; Zhao, Y. F.; Chen, M.; Wang, Q. P.; Qu, Y. T. et al. Construction of highly accessible single Co site catalyst for glucose detection. *Sci. Bull.* 2020, *65*, 2100–2106.

[5] Wang, Q. P.; Chen, M.; Xiong, C.; Zhu, X. F.; Chen, C.; Zhou, F. Y.; Dong, Y.; Wang, Y.; Xu, J.; Li, Y. M. et al. Dual confinement of high-loading enzymes within metal-organic frameworks for glucose sensor with enhanced cascade biocatalysis. *Biosens. Bioelectron.* 2022, *196*, 113695.

[6] Zhang, S. M.; Cicoira, F. Flexible self-powered biosensors. *Nature* 2018, *561*, 466–467.

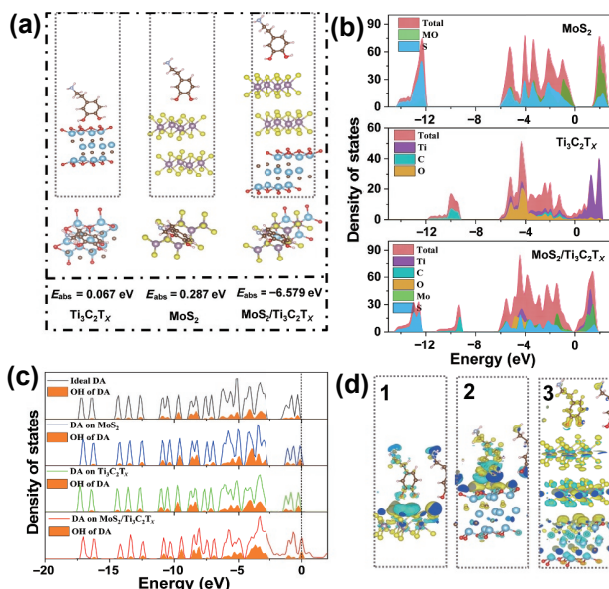[7] Condon, M. D.; Platt, N. J.; Zhang, Y. F.; Roberts, B. M.; Clements,

M. A.; Vietti-Michelina, S.; Tseu, M. Y.; Brimblecombe, K. R.; Threlfell, S.; Mann, E. O. et al. Plasticity in striatal dopamine release is governed by release-independent depression and the dopamine transporter. *Nat. Commun.* **2019**, *10*, 4263.

[8] Xiao, Y. S.; Wang, J. Dopamine: Opening the door of movement. *Mov. Disord.* **2018**, *33*, 1269.

[9] Larsen, B.; Olafsson, V.; Calabro, F.; Laymon, C.; Tervo-Clemmens, B.; Campbell, E.; Minhas, D.; Montez, D.; Price, J.; Luna, B. Maturation of the human striatal dopamine system revealed by PET and quantitative MRI. *Nat. Commun.* **2020**, *11*, 846.

[10] Njagi, J.; Chernov, M. M.; Leiter, J. C.; Andreescu, S. Amperometric detection of dopamine *in vivo* with an enzyme based carbon fiber microbiosensor. *Anal. Chem.* **2010**, *82*, 989–996.

[11] Zhang, J. L.; Wang, Y. H.; Huang, K.; Huang, K. J.; Jiang, H.; Wang, X. M. Enzyme-based biofuel cells for biosensors and *in vivo* power supply. *Nano Energy* **2021**, *84*, 105853.

[12] Alagiri, M.; Rameshkumar, P.; Pandikumar, A. Gold nanorod-based electrochemical sensing of small biomolecules: A review. *Microchim. Acta* **2017**, *184*, 3069–3092.

[13] He, W. Z.; Liu, R. T.; Zhou, P.; Liu, Q. Y.; Cui, T. H. Flexible micro-sensors with self-assembled graphene on a polyolefin substrate for dopamine detection. *Biosens. Bioelectron.* **2020**, *167*, 112473.

[14] Ramachandran, R.; Leng, X. H.; Zhao, C. H.; Xu, Z. X.; Wang, F. 2D siloxene sheets: A novel electrochemical sensor for selective dopamine detection. *Appl. Mater. Today* **2020**, *18*, 100477.

[15] Lei, Y.; Butler, D.; Lucking, M. C.; Zhang, F.; Xia, T. A.; Fujisawa, K.; Granzier-Nakajima, T.; Cruz-Silva, R.; Endo, E.; Terrones, H. et al. Single-atom doping of MoS_2 with manganese enables ultrasensitive detection of dopamine: Experimental and computational approach. *Sci. Adv.* **2020**, *6*, eabc4250.

[16] Ahmadi, N.; Bagherzadeh, M.; Nemati, A. Comparison between electrochemical and photoelectrochemical detection of dopamine based on titania-ceria-graphene quantum dots nanocomposite. *Biosens. Bioelectron.* **2020**, *151*, 111977.

[17] Verma, S.; Arya, P.; Singh, A.; Kaswan, J.; Shukla, A.; Kushwaha, H. R.; Gupta, S.; Singh, S. P. ZnO-rGO nanocomposite based bioelectrode for sensitive and ultrafast detection of dopamine in human serum. *Biosens. Bioelectron.* **2020**, *165*, 112347.

[18] Liu, N.; Xiang, X. P.; Fu, L.; Cao, Q.; Huang, R.; Liu, H.; Han, G.; Wu, L. D. Regenerative field effect transistor biosensor for *in vivo* monitoring of dopamine in fish brains. *Biosens. Bioelectron.* **2021**, *188*, 113340.

[19] Sajid, M.; Baig, N.; Alhooshani, K. Chemically modified electrodes for electrochemical detection of dopamine: Challenges and opportunities. *TrAC Trends Anal. Chem.* **2019**, *118*, 368–385.

[20] Gong, Q. J.; Han, H. X.; Wang, Y. D.; Yao, C. Z.; Yang, H. Y.; Qiao, J. L. An electrochemical sensor for dopamine detection using poly-tryptophan composited graphene on glassy carbon as the electrode. *New Carbon Mater.* **2020**, *35*, 34–41.

[21] Song, H. S.; Kwon, O. S.; Kim, J. H.; Conde, J.; Artzi, N. 3D hydrogel scaffold doped with 2D graphene materials for biosensors and bioelectronics. *Biosens. Bioelectron.* **2017**, *89*, 187–200.

[22] Tutar, R.; Motealleh, A.; Khademhosseini, A.; Kehr, N. S. Functional nanomaterials on 2D surfaces and in 3D nanocomposite hydrogels for biomedical applications. *Adv. Funct. Mater.* **2019**, *29*, 1904344.

[23] Li, B.; Gil, B.; Power, M.; Gao, A. Z.; Treratanakulchai, S.; Anastasova, S.; Yang, G. Z. Carbon-nanotube-coated 3D microspring force sensor for medical applications. *ACS Appl. Mater. Interfaces* **2019**, *11*, 35577–35586.

[24] Lu, D. X.; Li, J. H.; Wu, Z.; Yuan, L.; Fang, W. H.; Zou, P.; Ma, L.; Wang, X. J. High-activity daisy-like zeolitic imidazolate framework-67/reduced grapheme oxide-based colorimetric biosensor for sensitive detection of hydrogen peroxide. *J. Colloid Interface Sci.* **2022**, *608*, 3069–3078.

[25] Zhou, J. D.; Lin, J. H.; Huang, X. W.; Zhou, Y.; Chen, Y.; Xia, J.; Wang, H.; Xie, Y.; Yu, H. M.; Lei, J. C. et al. A library of atomically thin metal chalcogenides. *Nature* **2018**, *556*, 355–359.

[26] Kwon, K. C.; Baek, J. H.; Hong, K.; Kim, S. Y.; Jang, H. W. Correction to: Memristive devices based on two-dimensional transition metal chalcogenides for neuromorphic computing. *Nano-Micro Lett.* **2022**, *14*, 71.

[27] Luo, P.; Zhuge, F. W.; Zhang, Q. F.; Chen, Y. Q.; Lv, L.; Huang, Y.; Li, H. Q.; Zhai, T. Y. Doping engineering and functionalization of two-dimensional metal chalcogenides. *Nanoscale Horiz.* **2019**, *4*, 26–51.

[28] Lei, S. D.; Wang, X. F.; Li, B.; Kang, J. H.; He, Y. M.; George, A.; Ge, L. H.; Gong, Y. J.; Dong, P.; Jin, Z. H. et al. Surface functionalization of two-dimensional metal chalcogenides by Lewis acid-base chemistry. *Nat. Nanotechnol.* **2016**, *11*, 465–471.

[29] Wang, Y. C.; Ren, B. Y.; Ou, J. Z.; Xu, K.; Yang, C. H.; Li, Y. X.; Zhang, H. J. Engineering two-dimensional metal oxides and chalcogenides for enhanced electro-and photocatalysis. *Sci. Bull.* **2021**, *66*, 1228–1252.

[30] Vancsó, P.; Popov, Z. I.; Pető, J.; Ollár, T.; Dobrik, G.; Pap, J. S.; Hwang, C.; Sorokin, P. B.; Tapasztó, L. Transition metal chalcogenide single layers as an active platform for single-atom catalysis. *ACS Energy Lett.* **2019**, *4*, 1947–1953.

[31] Chou, S. S.; De, M.; Kim, J.; Byun, S.; Dykstra, C.; Yu, J.; Huang, J. X.; Dravid, V. P. Ligand conjugation of chemically exfoliated MoS_2. *J. Am. Chem. Soc.* **2013**, *135*, 4584–4587.

[32] Lu, J. P.; Lu, J. H.; Liu, H. W.; Liu, B.; Gong, L. L.; Tok, E. S.; Loh, K. P.; Sow, C. H. Microlandscaping of Au nanoparticles on few-layer MoS_2 films for chemical sensing. *Small* **2015**, *11*, 1792–1800.

[33] Karimipour, M.; Khazraei, S.; Kim, B. J.; Boschloo, G.; Johansson, E. M. J. Efficient and bending durable flexible perovskite solar cells via interface modification using a combination of thin MoS_2 nanosheets and molecules binding to the perovskite. *Nano Energy* **2022**, *95*, 107044.

[34] Mitterreiter, E.; Schuler, B.; Micevic, A.; Hernangómez-Pérez, D.; Barthelmi, K.; Cochrane, K. A.; Kiemle, J.; Sigger, F.; Klein, J.; Wong, E. et al. The role of chalcogen vacancies for atomic defect emission in MoS_2. *Nat. Commun.* **2021**, *12*, 3822.

[35] Wang, X.; Zhang, Y. W.; Si, H. N.; Zhang, Q. H.; Wu, J.; Gao, L.; Wei, X. F.; Sun, Y.; Liao, Q. L.; Zhang, Z. et al. Single-atom vacancy defect to trigger high-efficiency hydrogen evolution of MoS_2. *J. Am. Chem. Soc.* **2020**, *142*, 4298–4308.

[36] Li, D. Y.; Zhao, L. L.; Xia, Q.; Wang, J.; Liu, X. M.; Xu, H. R.; Chou, S. L. Activating MoS_2 Nanoflakes via Sulfur Defect Engineering Wrapped on CNTs for Stable and Efficient Li-O_2 Batteries. *Adv. Funct. Mater.* **2022**, *32*, 2108153.

[37] Yilmaz, G.; Yang, T.; Du, Y. H. Yu, X. J.; Feng, Y. P.; Shen, L.; Ho, G. W. Stimulated electrocatalytic hydrogen evolution activity of MOF-derived MoS_2 basal domains via charge injection through surface functionalization and heteroatom doping. *Adv. Sci.* **2019**, *6*, 1900140.

[38] Zhu, H. Y.; Gan, X.; McCreary, A.; Lv, R. T.; Lin, Z.; Terrones, M. Heteroatom doping of two-dimensional materials: From graphene to chalcogenides. *Nano Today* **2020**, *30*, 100829.

[39] Yang, W. W.; Zhang, S. Q.; Chen, Q.; Zhang, C.; Wei, Y.; Jiang, H. N.; Lin, Y. X.; Zhao, M. T.; He, Q. Q.; Wang, X. G. et al. Conversion of intercalated MoO_3 to multi-heteroatoms-doped MoS_2 with high hydrogen evolution activity. *Adv. Mater.* **2020**, *32*, 2001167.

[40] Liu, F. R.; Wang, N.; Shi, C. S.; Sha, J. W.; Ma, L. Y.; Liu, E. Z.; Zhao, N. Q. Phosphorus doping of 3D structural MoS_2 to promote catalytic activity for lithium-sulfur batteries. *Chem. Eng. J.* **2022**, *431*, 133923.

[41] Lu, T. Y.; Li, T. F.; Shi, D. S.; Sun, J. L.; Pang, H.; Xu, L.; Yang, J.; Tang, Y. W. *In situ* establishment of Co/MoS_2 heterostructures onto inverse opal-structured N, S-doped carbon hollow nanospheres: Interfacial and architectural dual engineering for efficient hydrogen evolution reaction. *SmartMat* **2021**, *2*, 591–602.

[42] Wang, S. H.; Wang, L. L.; Xie, L. B.; Zhao, W. W.; Liu, X.; Zhuang, Z. C.; Zhuang, Y. L.; Chen, J.; Liu, S. J.; Zhao, Q. Dislocation-strained MoS_2 nanosheets for high-efficiency hydrogen evolution reaction. *Nano Res.* **2022**, *15*, 4996–5003.

[43] Huang, Y. L.; Chen, W.; Wee, A. T. S. Two-dimensional magnetic transition metal chalcogenides. *SmartMat* **2021**, *2*, 139–153.

[44] Jiang, K.; Luo, M.; Liu, Z. Z.; Peng, M.; Chen, D. C.; Lu, Y. R.; Chan, T. S.; De Groot, F. M. F.; Tan, Y. W. Rational strain engineering of single-atom ruthenium on nanoporous MoS_2 for

highly efficient hydrogen evolution. *Nat. Commun.* **2021**, *12*, 1687.

[45] Liu, D. B.; Xu, W. Y.; Liu, Q.; He, Q.; Haleem, Y. A.; Wang, C. D.; Xiang, T.; Zou, C. W.; Chu, W. S.; Zhong, J. et al. Unsaturated-sulfur-rich MoS$_2$ nanosheets decorated on free-standing SWNT film: Synthesis, characterization and electrocatalytic application. *Nano Res.* **2016**, *9*, 2079–2087.

[46] Feng, Y. Y.; Zhang, T.; Zhang, J. H.; Fan, H.; He, C.; Song, J. X. 3D 1T-MoS$_2$/CoS$_2$ heterostructure via interface engineering for ultrafast hydrogen evolution reaction. *Small* **2020**, *16*, 2002850.

[47] Sun, X.; Deng, H. T.; Zhu, W. G.; Yu, Z.; Wu, C. Z.; Xie Y. Interface engineering in two-dimensional heterostructures: Towards an advanced catalyst for ullmann couplings. *Angew. Chem., Int. Ed,* **2016**, *55*, 1704–1709.

[48] Lu, X. L.; Xu, K.; Tao, S.; Shao, Z. W.; Peng, X.; Bi, W. T.; Chen, P. Z.; Ding, H.; Chu, W. S.; Wu, C. Z. et al. Engineering the electronic structure of two-dimensional subnanopore nanosheets using molecular titanium-oxide incorporation for enhanced photocatalytic activity. *Chem. Sci.* **2016**, *7*, 1462–1467.

[49] Kamysbayev, V.; Filatov, A. S.; Hu, H. C.; Rui, X.; Lagunas, F.; Wang, D.; Klie, R. F.; Talapin, D. V. Covalent surface modifications and superconductivity of two-dimensional metal carbide MXenes. *Science* **2020**, *369*, 979–983.

[50] Zou, J.; Wu, J.; Wang, Y. Z.; Deng, F. X.; Jiang, J. Z.; Zhang, Y. Z.; Liu, S.; Zhang, H.; Yu, J. G.; Zhai, T. Y. et al. Additive-mediated intercalation and surface modification of MXenes. *Chem. Soc. Rev.* **2022**, *51*, 2972–2990.

[51] Wang, J. Q.; Liu, L.; Jiao, S. L.; Ma, K. J.; Lv, J.; Yang, J. J. Hierarchical carbon Fiber@MXene@MoS$_2$ core-sheath synergistic microstructure for tunable and efficient microwave absorption. *Adv. Funct. Mater.* **2020**, *30*, 2002595.

[52] Gao, Y. Y.; Liu, G. X.; Bu, T. Z.; Liu, Y. Y.; Qi, Y. C.; Xie, Y. T.; Xu, S. H.; Deng, W. L.; Yang, W. Q.; Zhang, C. MXene based mechanically and electrically enhanced film for triboelectric nanogenerator. *Nano Res.* **2021**, *14*, 4833–4840.

[53] Sun, Y.; Zhou, Y. J.; Liu, Y.; Wu, Q. Y.; Zhu, M. M.; Huang, H.; Liu, Y.; Shao, M. W.; Kang, Z. H. A photoactive process cascaded electrocatalysis for enhanced methanol oxidation over Pt-MXene-TiO$_2$ composite. *Nano Res.* **2020**, *13*, 2683–2690.

[54] Zhu, J. T.; Wang, H.; Ma, L.; Zou, G. F. Observation of ambipolar photoresponse from 2D MoS$_2$/MXene heterostructure. *Nano Res.* **2021**, *14*, 3416–3422.

[55] Luo, Y. J.; Shen, P.; Li, X. C.; Guo, Y. L.; Chu, K. Sulfur-deficient Bi$_2$S$_{3-x}$ synergistically coupling Ti$_3$C$_2$T$_x$-MXene for boosting electrocatalytic N$_2$ reduction. *Nano Res.* **2022**, *15*, 3991–3999.

[56] Zhang, S. L.; Ying, H. J.; Huang, P. F.; Wang, J. L.; Zhang, Z.; Yang, T. T.; Han, W. Q. Rational design of pillared SnS/Ti$_3$C$_2$T$_x$ MXene for superior lithium-ion storage. *ACS Nano* **2020**, *14*,

17665–17674.

[57] Yuan, Z. Y.; Wang, L. L.; Li, D. D.; Cao, J. M.; Han, W. Carbon-reinforced Nb$_2$CT$_x$ MXene/MoS$_2$ nanosheets as a superior rate and high-capacity anode for sodium-ion batteries. *ACS Nano* **2021**, *15*, 7439–7450.

[58] Ma, K.; Dong, Y. R.; Jiang, H.; Hu, Y. J.; Saha, P.; Li, C. Z. Densified MoS$_2$/Ti$_3$C$_2$ films with balanced porosity for ultrahigh volumetric capacity sodium-ion battery. *Chem. Eng. J.* **2020**, *413*, 127479.

[59] Chang, Y. H.; Lin, C. T.; Chen, T. Y.; Hsu, C. L.; Lee, Y. H.; Zhang, W. J.; Wei, K. H.; Li, L. J. Highly efficient electrocatalytic hydrogen production by MoS$_x$ grown on graphene-protected 3D Ni foams. *Adv. Mater.* **2013**, *25*, 756–760.

[60] Liang, X.; Garsuch, A.; Nazar, L. F. Sulfur cathodes based on conductive MXene nanosheets for high-performance lithium-sulfur batteries. *Angew. Chem., Int. Ed.* **2015**, *54*, 3907–3911.

[61] Deng, S. X.; Wang, B. Q.; Yuan, Y. F.; Li, X.; Sun, Q.; Doyle-Davis, K.; Banis, M. N.; Liang, J. N.; Zhao, Y.; Li, J. J. et al. Manipulation of an ionic and electronic conductive interface for highly-stable high-voltage cathodes. *Nano Energy* **2019**, *65*, 103988–103997.

[62] Chen, W. X.; Pei, J. J.; He, C. T.; Wan, J. W.; Ren, H. L.; Zhu, Y. Q.; Wang, Y.; Dong, J. C.; Tian, S. B.; Cheong, W. C. et al. Rational design of single molybdenum atoms anchored on N-Doped carbon for effective hydrogen evolution reaction. *Angew. Chem., Int. Ed.* **2017**, *56*, 16086–16090.

[63] Liu, Q.; Fang, Q.; Chu, W. S.; Wan, Y. Y.; Li, X. L.; Xu, W. Y.; Habib, M.; Tao, S.; Zhou, Y.; Liu, D. B. et al. Electron-Doped 1T-MoS$_2$ via interface engineering for enhanced electrocatalytic hydrogen evolution. *Chem. Mater.* **2017**, *29*, 4738–4744.

[64] Xu, H.; Yi, J. J.; She, X. J.; Liu, Q.; Song, L.; Chen, S. M.; Yang, Y. C.; Song, Y. H.; Vajtai, R.; Lou, J. et al. 2D heterostructure comprised of metallic 1T-MoS$_2$ /Monolayer O-g-C$_3$N$_4$ towards efficient photocatalytic hydrogen evolution. *Appl. Catal. B:Environ.* **2018**, *220*, 379–385.

[65] Ryaboshapka, D.; Piccolo, L.; Aouine, M.; Bargiela, P.; Briois, V.; Afanasiev, P. Ultradispersed (Co)Mo catalysts with high hydrodesulfurization activity. *Appl. Catal. B:Environ.* **2022**, *302*, 120831.

[66] Li, Q.; Huo, C. R.; Yi, K.; Zhou, L. L.; Su, L.; Hou, X. M. Preparation of flake hexagonal BN and its application in electrochemical detection of ascorbic acid, dopamine and uric acid. *Sensors Actuat. B:Chem.* **2018**, *260*, 346–356.

[67] Xi, X.; Wu, D. Q.; Ji, W.; Zhang, S. N.; Tang, W.; Su, Y. Z.; Guo, X. J.; Liu, R. L. Manipulating the sensitivity and selectivity of OECT-based biosensors via the surface engineering of carbon cloth gate electrodes. *Adv. Funct. Mater.* **2020**, *30*, 1905361.